IceSound: Acoustic-based Ice Thickness Sensing with Smartphones

CHI LIN*, School of Software Technology, Dalian University of Technology, China
YINGQI CHEN, School of Software Technology, Dalian University of Technology, China
JIE XIONG, College of Computing and Data Science, Nanyang Technological University, Singapore
YANG CHI, School of Software Technology, Dalian University of Technology, China
XIN FAN, School of Software Technology, Dalian University of Technology, China
QIANG TONG, Lenovo, China
GUOWEI WU, School of Software Technology, Dalian University of Technology, China

Accurate measurement of ice thickness is essential for safety in ice-related human activities; however, existing solutions are often cumbersome or expensive. We present IceSound, a novel system that leverages the ubiquity of smartphones to realize portable, cost-effective, and real-time ice thickness sensing. IceSound tackles multiple challenges including overlapping echoes due to the higher sound speed in ice (approximately 3250 m/s), weak bottom reflections due to attenuation in thick ice, and variations of temperature and device orientation during measurements. Extensive field experiments show that IceSound achieves a mean absolute error of 0.3 cm for ice thickness measurement when the ice thickness is in the critical range of 10-15 cm. When assessing whether the ice thickness is safe for human activities based on the well-recognized 15 cm threshold, the system exhibits a remarkably low error rate of 0.13%, demonstrating its effectiveness in enhancing safety for ice-related human activities.

CCS Concepts: • **Human-centered computing** → **Ubiquitous and mobile computing**.

Additional Key Words and Phrases: Acoustic Sensing, Mobile Computing, Smartphone

ACM Reference Format:
Chi Lin, Yingqi Chen, Jie Xiong, Yang Chi, Xin Fan, Qiang Tong, and Guowei Wu. 2025. IceSound: Acoustic-based Ice Thickness Sensing with Smartphones. *Proc. ACM Interact. Mob. Wearable Ubiquitous Technol.* 9, 3, Article 109 (September 2025), 25 pages. https://doi.org/10.1145/3749543

1 INTRODUCTION

Accurate and real-time measurement of ice thickness is vital for ensuring safety for ice-related human activities, such as river skating and ice fishing. Each year, a large number of accidents occur due to misjudgment of ice conditions, leading to approximately 2000 deaths [37]. Traditional manual measurement methods rely on ice augers or chisels to drill holes and measure the thickness of the ice with a tape measure or specialized probes [28]. These methods are labor-intensive, time-consuming, and unsuitable for thick ice [39]. Another common approach

*Corresponding author.

Authors' Contact Information: Chi Lin, School of Software Technology, Dalian University of Technology, Dalian, China, c.lin@dlut.edu.cn; Yingqi Chen, School of Software Technology, Dalian University of Technology, Dalian, China, 1005658400@mail.dlut.edu.cn; Jie Xiong, College of Computing and Data Science, Nanyang Technological University, Singapore, Singapore, jxiong@cs.umass.edu; Yang Chi, School of Software Technology, Dalian University of Technology, Dalian, China, chiyang@mail.dlut.edu.cn; Xin Fan, School of Software Technology, Dalian University of Technology, Dalian, China, xin.fan@dlut.edu.cn; Qiang Tong, Lenovo, Beijing, China, tongqiang2@lenovo.com; Guowei Wu, School of Software Technology, Dalian University of Technology, Dalian, China, wgwdut@dlut.edu.cn.

Permission to make digital or hard copies of all or part of this work for personal or classroom use is granted without fee provided that copies are not made or distributed for profit or commercial advantage and that copies bear this notice and the full citation on the first page. Copyrights for third-party components of this work must be honored. For all other uses, contact the owner/author(s).
© 2025 Copyright held by the owner/author(s).
ACM 2474-9567/2025/9-ART109
https://doi.org/10.1145/3749543

is adopting ground-penetrating radar (GPR) to measure ice thickness by transmitting electromagnetic waves and analyzing the reflected signals [11]. While GPR can provide real-time ice thickness measurements, the equipment is prohibitively expensive ($15,000 to $100,000) and it requires trained professional for operation. Thermal imaging technique has also been employed for ice thickness estimation leveraging temperature differences between ice and water surfaces [43]. However, this method is susceptible to environmental interference and the achieved accuracy is low. Note that laser-based distance meters, commonly used for measuring distances and thicknesses, are not suitable for ice thickness measurement. The laser beam has difficulties to penetrate the ice, with most of its power reflected by the ice surface [31]. In this work, for the first time, we propose to use acoustic signals emitted from commercial smartphones for ice thickness measurement. Compared to existing solutions, the proposed system offers significant advantages in terms of portability and cost. While promising, realizing accurate ice thickness measurement with commercial smartphones faces multiple challenges:

- **Overlapping echoes:** While the speed of sound in the air is around 340 m/s, the propagation speed in ice is much larger (around 3250 m/s). This larger speed brings a unique challenge for ice thickness measurement as it decreases resolution by causing sound to travel farther within the same time interval. This leads to possible overlapping of reflections from the top air-ice and bottom ice-water interfaces, making it difficult to accurately determine the ice thickness.
- **Weak bottom echo:** The thickness of commonly-seen ice varies significantly, ranging from a few centimeters to tens of centimeters. For thick ice, the bottom ice-water echo is very weak due to significant signal attenuation in the ice. This makes extracting information from the bottom ice-water echo for measurement challenging.
- **Temperature and orientation variations:** Two practical factors severely affect the performance of ice thickness measurement. The first practical factor is the dramatic temperature variations in outdoor environments. The propagation speed of sound in ice varies significantly with temperature: from 3250 m/s at 0 °C (near water interface) to 3800 m/s at -30 °C. What makes the situation more complicated is that the temperature of ice is not uniform but varies from the top surface (i.e., air temperature) to the bottom surface (i.e., 0 °C), leading to a non-negligible error if a constant sound speed is assumed. The second practical factor affecting the sensing performance is the smartphone's orientation towards the ice. It is not practical to require the user to point the smartphone at exactly 90° towards the ice surface for measurement. This orientation deviation also affects the measurement accuracy.

To address the aforementioned challenges, we propose IceSound, a novel smartphone-based acoustic system for accurate ice thickness measurement. As shown in Figure 1, IceSound provides real-time ice thickness measurements through a mobile app, utilizing the smartphone's built-in speakers and microphones to prevent dangerous ice breaking accidents during winter activities.

To address the first challenge, we utilize the largest possible bandwidth on the smartphone for the chirp signal design to improve distance resolution. We choose the frequency range as 3-22 kHz. The lower boundary is chosen as 3 kHz to avoid low-frequency acoustic interference from the environment. The highest frequency a smartphone can support is usually 24 kHz. However, as the frequency response becomes unstable beyond 22 kHz [11], we choose the upper boundary as 22 kHz.

To address the second challenge of extremely weak signal when the ice is thick, we first develop delicate designs including high-pass filter, wavelet denosing and fusion of multiple measurements to remove various types of noise. Then, instead of only applying the conventional Short-Time Fourier Transform (STFT), we also combine the correlation technique in the time-domain which is effective in extracting the distance information from weak echoes.

To address the issue of temperature variation, we quantitatively model the non-linear distribution of temperature within the ice and the corresponding detailed sound speed information. Our system leverages public-available

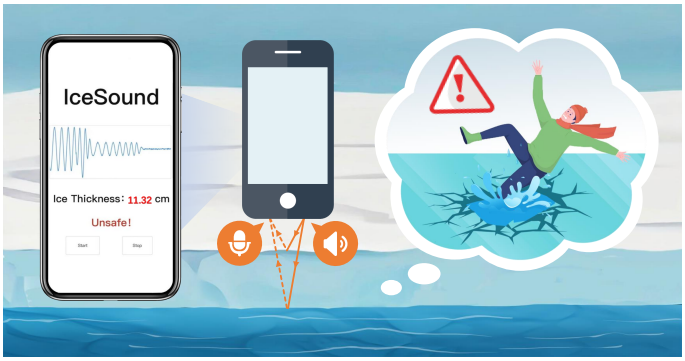

Fig. 1. A diagram of IceSound application scenarios.

weather APIs to obtain real-time temperature and solar radiation data for accurate ice surface temperature estimation. For orientation compensation, we employ the sensor readings from the smartphone and fuse information from the accelerometer and magnetometer to estimate and correct the device tilt. These methods significantly improve the performance of the proposed system in terms of accuracy, robustness and practicality.

The main contributions of our work are as follows:

- To the best of our knowledge, this is the first system that utilizes smartphones for measuring ice thickness, offering a novel and practical method for portable ice thickness measurement.
- We tackle technical challenges like weak bottom echoes, as well as practical issues such as temperature and orientation variations, to ensure that our proposed system is both practical and robust for real-world ice thickness measurements.
- We implement the IceSound on various commodity smartphones, demonstrating the feasibility of the proposed approach through extensive experiments in both lab environment and in the wild. Our comprehensive experiments show that the system achieves a mean absolute error of 0.3 cm in real-world outdoor environments when the ice thickness is in the critical range of 10-15 cm, and a notably low error rate of 0.13% when judging if the ice is safe for human activities,[1] validating the effectiveness and practicality of the proposed approach.

2 PRELIMINARIES

2.1 Theoretical Resolution in Acoustic Measurement

The fundamental principle behind acoustic-based ice thickness measurement is the reflection of sound waves at interfaces between different media [38]. In our system, we utilize the reflections that occur at the air-ice and ice-water interfaces. The time delay between these reflections, combined with the known speed of sound in ice, allows us to calculate the ice thickness.

The theoretical distance resolution of our system is given by: $\Delta r \approx \frac{c}{2B}$, where Δr is the distance resolution, c is the speed of sound in ice (approximately 3250 m/s), and B is the bandwidth of the acoustic signal [7]. This formula is derived from the principles of signal processing and wave propagation [40]. Specifically, the ability to resolve two closely spaced reflections is directly related to the shortest pulse we can generate [5]. In the time-domain, the pulse width Δt is inversely proportional to the bandwidth B, expressed as $\Delta t \approx 1/B$ [21].

[1]Whether the ice is safe for human activities is judged based on the well-recognized ice thickness threshold, i.e., a thickness above 15 cm is safe for human activities.

In ice, the propagation distance is calculated as $\Delta r = c\Delta t$ [15]. We can thus derive the resolution formula: $\Delta r = c\Delta t \approx c \cdot \frac{1}{2B} = \frac{c}{2B}$, This relationship shows that to achieve finer distance resolution (smaller Δr), we need to increase the bandwidth B of our signal [50]. A larger bandwidth allows for shorter pulse widths in the time-domain, enabling the system to distinguish between closely spaced reflections [32]. In the context of ice thickness measurement, this resolution determines our ability to distinguish signals reflected from the two surfaces of the ice [25]. For instance, with a bandwidth of 19 kHz (as in our system), we can theoretically achieve a resolution of: $\Delta r \approx \frac{3250\ \text{m/s}}{2 \cdot 19000\ \text{Hz}} \approx 0.085$ m = 8.5 cm. This theoretical limit guides our system design and helps us understand the capabilities and limitations of our acoustic-based ice thickness measurement approach [33].

2.2 Smartphone Microphone Sampling Mechanism

Smartphone microphones employ analog-to-digital converters (ADCs) to transform continuous sound waves into discrete digital signals [12]. This process begins with the collection of sound waves by the microphone's diaphragm, a thin, flexible material that vibrates in response to changes in air pressure. The mechanical vibrations of the diaphragm are then converted into electrical signals by a transducer within the microphone [13]. These weak electrical signals are amplified and processed before entering the ADC for digitization.

The digitization process involves two key concepts: sampling rate and bit depth [46]. The sampling rate, typically measured in Hertz (Hz), refers to the number of samples taken per second. Most modern smartphones offer a maximum sampling rate of 48 kHz, meaning they can capture 48,000 samples per second [12]. Bit depth, on the other hand, determines how precisely the amplitude of the sound wave is measured. Common bit depths in smartphones are 16-bit or 24-bit, providing 65,536 or over 16 million possible amplitude values, respectively [29].

During the analog-to-digital conversion, the continuous analog signal is sampled at discrete time intervals determined by the sampling rate. Each sample is then quantized to the nearest predefined digital level based on the bit depth [18]. This process inevitably introduces some quantization error, which is reduced with higher bit depths. The resulting digital values are encoded into binary data, which can be compressed and stored using various audio encoding formats such as Waveform Audio File Format (WAV), Advanced Audio Coding (AAC), or Moving Picture Experts Group Layer-3 Audio (MP3) [47].

In IceSound, we leverage the sampling rates and bit depths available in modern smartphones to capture acoustic information, which allows us to measure accurate ice thickness.

2.3 Acoustic Wave Propagation in Ice

The accurate measurement of ice thickness through acoustic methods requires a comprehensive understanding of sound wave behavior in ice. The speed of sound in ice exhibits notable temperature dependence, with a reference value of approximately 3250 m/s at 0 °C. This temperature sensitivity is attributed to the molecular dynamics of ice structures and their response to thermal variations, which directly affects the propagation of mechanical vibrations [14]. Sound propagation in ice is influenced by several temperature-related factors [20]. Thermal gradients within ice layers can create variations in acoustic properties, where both the speed and attenuation of sound waves are modified by local temperature conditions [36]. Temperature fluctuations near the ice surface, often driven by diurnal cycles and weather patterns, affect the acoustic properties of the upper ice layers [35]. These thermal variations can lead to complex acoustic behavior that requires careful consideration in measurement applications [27].

Acoustic measurements in ice are subject to various forms of interference and noise, which can significantly impact the accuracy of thickness measurements [30]. Scattering is a primary concern, caused by inhomogeneities in the ice such as cracks, air bubbles, or impurities [10]. Absorption of acoustic energy by the ice, converting it to heat, is another significant factor, particularly for higher frequency signals. This absorption process is frequency-dependent and generally increases with the frequency of the acoustic waves.

3 SYSTEM DESIGN

3.1 Design Overview

The IceSound system implements a comprehensive signal processing pipeline for ice thickness measurement using commodity smartphones. At its core, the system transmits a chirp signal (3-22 kHz) through the smartphone's speaker and captures the return signal via its microphone. This dual-channel acoustic sensing approach enables precise ice thickness measurements, from thin layers to formations over one meter thick. To determine ice thickness, the system applies the fundamental time-of-flight principle, which can be expressed as:

$$d = \frac{v_{\text{ice}} \cdot \Delta t}{2 \cos \theta}, \tag{1}$$

where d represents ice thickness, v_{ice} is the sound speed in ice, Δt is the time delay between surface and bottom echoes, and θ is the incident angle of the acoustic signal.

The return signal undergoes multi-stage denoising to eliminate environmental interference, as shown in Figure 2. For echo analysis, IceSound employs time-domain methods for thicker ice with distinct echoes and frequency-domain analysis for thin ice with overlapping reflections. These approaches accurately determine the time delay Δt between echoes.

A compensation module adjusts for device orientation and temperature effects, optimizing both incident angle θ and sound speed v_{ice} parameters. Through rigorous validation, IceSound achieves ±0.3 cm accuracy, providing real-time thickness measurements and safety assessments.

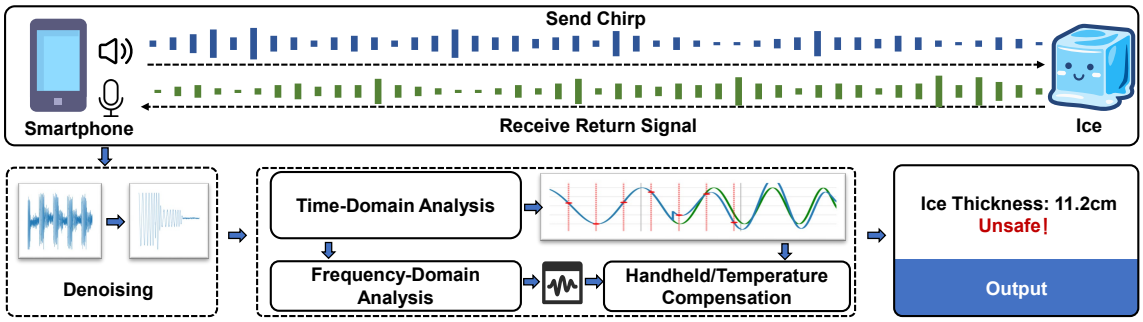

Fig. 2. System design.

3.2 Chirp Design

3.2.1 Frequency Range. Determining the appropriate frequency range is critical for balancing penetration depth and resolution. After extensive experimentation, we selected a frequency range of 3-22 kHz. This wide bandwidth is crucial for achieving high time resolution, as explained by the relationship $\Delta t \approx 1/B$, where Δt is the time resolution and B is the bandwidth. This relationship implies that a wider bandwidth allows for better time resolution, which is essential for accurate thickness estimation.

Our analysis shows that 96% of the wind noise and ice-internal noise is distributed below 2.5 kHz. While a highpass filter with a 2.5 kHz cutoff frequency could remove most of this noise, we must consider the transition width of non-ideal filters. To prevent residual noise from overwhelming the real signal, we implement a 500 Hz guard band, setting our lower frequency bound to 3 kHz. The upper bound of 22 kHz is chosen to maximize the bandwidth within the limitations of smartphone hardware. By utilizing this selected frequency range, our system can provide high-resolution measurements while maintaining low noise.

3.2.2 Chirp Duration. The duration of the chirp is a critical parameter that affects both measurement accuracy and system efficiency. The selected excitation pattern employs 20 ms cycles consisting of 8 ms linear chirps (3-22 kHz) followed by 12 ms silent intervals, achieving a balance between signal energy and immunity to environmental noise. The short duration allows the system to capture multiple valid measurements within a brief time window, which is essential for real-time performance. At the same time, such a time duration is long enough to accumulate sufficient energy for reliable detection of the ice-water interface reflection. The 8 ms chirp offers an effective balance, enabling rapid data collection while ensuring reliable signal detection even under challenging ice conditions. By employing this carefully designed chirp, the system can rapidly collect and process multiple data points, delivering immediate and continuously updated ice thickness information to users.

3.3 Noise Reduction

Our ice thickness measurement system implements a systematic noise reduction strategy to ensure accurate measurements in complex ice environments. As shown in Figure 3, the denoising process consists of three sequential stages: high-pass filtering, wavelet denoising, and measurement fusion.

High-pass filtering. The raw signal $s(t)$ (Figure 3(a)) contains significant low-frequency noise, primarily from wind and ice vibrations. The inset shows a magnified view of the first 20 ms of the signal, highlighting the complex noise patterns in the initial echo response that could potentially mask the true ice-water interface reflections. We employ a high-pass filter with a cutoff frequency $f_c = 2$ kHz to effectively eliminate approximately 95% of wind-induced noise while preserving the chirp signal integrity. As illustrated in Figure 3(b), this initial filtering stage improves the Signal-to-Noise Ratio (SNR) by 7 dB.

Wavelet denoising. To address the noise from ice bubbles and impurities, we apply a wavelet-based denoising approach (Figure 3(c)). The system utilizes a 4-level discrete wavelet transform (DWT) with Daubechies-4 wavelets, followed by adaptive thresholding. This stage effectively isolates and reduces high-frequency perturbations while preserving essential structural features of the ice-water interface signal. The wavelet denoising process further enhances the SNR by an additional 3-5 dB.

Measurement fusion. Despite the effectiveness of the preceding stages, random noise—such as friction between the smartphone and gloves or ambient human-generated sounds—remains present in individual measurements. To mitigate this, we implement a measurement fusion technique (Figure 3(d)) that performs five rapid consecutive measurements within a 100 ms window. A magnified view of the first 20 ms of the processed signal reveals a significant improvement in clarity, with the initial echo now exhibiting distinct reflection patterns characteristic of the ice–water interface. This brief time frame is carefully selected to account for the unique properties of ice structures, ensuring stable ice conditions throughout the measurement sequence while capturing sufficient signal variations for effective noise filtering. These measurements are combined using a weighted median filter, with weights dynamically assigned based on two key factors specifically designed for ice thickness measurement:

(1) Signal strength — measurements with stronger return signals are assigned higher weights, as they indicate better acoustic coupling with the ice–water interface, and
(2) Consistency with neighboring measurements — measurements that closely align with adjacent readings are assigned higher weights, as they are more likely to reflect the true ice information rather than noise-induced outliers.

This approach improves measurement stability by 40% while maintaining real-time responsiveness with a processing delay of less than 0.3 s. The sequential improvement in signal quality is clearly visible in the time-domain waveforms shown in Figure 3(a)-(d), where the signal becomes progressively cleaner while maintaining its essential structural characteristics. This proposed three-stage noise reduction strategy shows promise in handling various noise sources while preserving critical signal features for ice thickness determination.

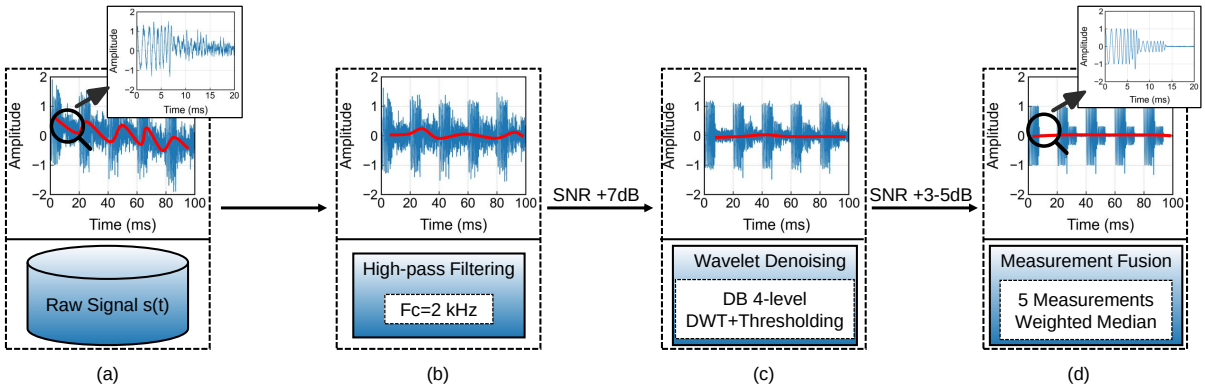

Fig. 3. The process of denoising.

3.4 Time-Domain Analysis

3.4.1 Mathematical Foundation. To establish a rigorous foundation for our ice thickness measurement system, we first develop a mathematical foundation that characterizes the acoustic signal propagation and echo detection process. This analytical model begins with the formulation of our chirp signal and its reflection at ice surfaces, providing the theoretical basis for subsequent parameter estimation and thickness calculation. First,we model our chirp signal as:

$$s(t) = \cos\left(2\pi\left(f_0 t + \frac{k}{2}t^2\right)\right), \tag{2}$$

where $f_0 = 3$ kHz is the initial frequency and $k = 2.375 \times 10^6$ Hz/s is the chirp rate. The recorded signal $y(t)$ includes the original signal and a delayed echo:

$$y(t) = s(t) + As(t - \tau), \tag{3}$$

where A is the attenuation coefficient and τ is the echo delay time. Sampling at times $t_1, t_2, \ldots, t_n$, we obtain:

$$y(t_i) = \cos\left(2\pi\left(f_0 t_i + \frac{k}{2}t_i^2\right)\right) + A\cos\left(2\pi\left(f_0(t_i - \tau) + \frac{k}{2}(t_i - \tau)^2\right)\right). \tag{4}$$

Since the echo from the upper ice surface consistently reaches the microphone before that of the lower surface, we begin our analysis by focusing on the first few samples. A gradient descent algorithm is employed to fit a non-linear chirp model to these initial sample points, specifically the first three. This choice allows us to precisely characterize the upper surface echo, as using at least three sample points ($n \geq 3$) is essential to uniquely determine the parameters A and τ.

This requirement arises because the chirp frequency varies with time, resulting in different phases at each sampling point t_i. With three or more properly spaced samples, we can capture this phase shift, providing enough information to accurately model the chirp. The non-linear nature of the equations makes an overdetermined system advantageous, as it yields stable solutions and better noise resilience. Mathematically, this is expressed in our objective function:

$$E(A, \tau) = \sum_{i=1}^{n}(y(t_i) - (\cos(2\pi(f_0 t_i + \frac{k}{2}t_i^2)) + A\cos(2\pi(f_0(t_i - \tau) + \frac{k}{2}(t_i - \tau)^2))))^2, \tag{5}$$

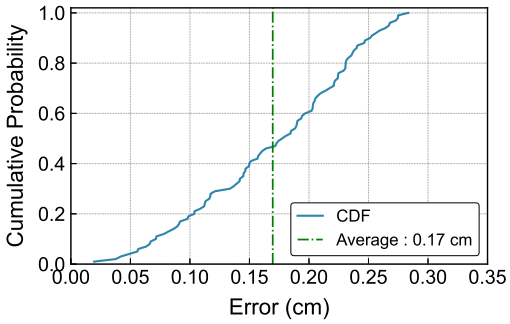

Fig. 4. The CDF plot of ice thickness measurement accuracy (IceSound).

where n denotes the number of sampling points. For $n = 1$, the system is underdetermined, leading to infinite solutions for A and τ. With $n = 2$, while determinable, the solution becomes highly sensitive to noise and non-linear behavior, risking local minima. In contrast, $n \geq 3$ provides an overdetermined system, improving robustness and convexity in the Hessian of $E(A, \tau)$ near the true values of A and τ. This leads to a more stable and accurate fit while reducing the risk of local extrema that could misrepresent the true solution.

3.4.2 Upper Surface Echo Fitting. Building upon our mathematical foundation, we now show how IceSound achieves sub-sampling measurement accuracy.

The theoretical resolution limit of our system—defined as the minimum distinguishable distance between two reflective surfaces—is determined by the signal bandwidth:

$$\Delta r = \frac{c_{\text{ice}}}{2B} = \frac{3250 \text{ m/s}}{2 \cdot 19000 \text{ Hz}} \approx 8.5 \text{ cm}. \tag{6}$$

Similarly, the nominal measurement accuracy based on the smartphone's 44 kHz sampling rate would be:

$$\Delta d = \frac{c_{\text{ice}}}{2f_s} = \frac{3250 \text{ m/s}}{2 \cdot 44000 \text{ Hz}} \approx 3.7 \text{ cm}. \tag{7}$$

As shown in Figure 4, the measured ice thickness accuracy is significantly higher than the theoretical value. This is because, for ice thickness determination, we leverage differential distance measurement between upper and lower surface reflections. The accuracy of distance difference measurements is fundamentally different from that of absolute distance measurements. A similar example is WiFi-based respiration sensing: although the absolute distance measurement accuracy of WiFi is typically on the order of several centimeters, displacement measurements (i.e., changes in distance) can achieve accuracies as fine as 1–2 millimeters—sufficient to capture subtle chest displacements (0.5 cm) for respiration monitoring [45, 48, 49]. By applying the proposed gradient descent optimization as illustrated in Figure 5 to the chirp signal, we achieve high precision ice thickness measurements.

As shown in Figure 5(a), what we can extract are the sampled values denoted as green dots. Note that the reflection from the upper layer of the ice reaches the microphone first, followed by the reflection from the lower layer. As a result, the first few sample points contain only the upper-layer reflection, while the subsequent sample points contain a combination of reflections from both layers. When the ice thickness is very thin (i.e., less than 8.5 cm), our system can identify that the thickness is below the safe threshold without needing to measure the exact thickness. We only perform a precise thickness measurement when the ice is thicker enough (e.g., >12 cm as the threshold thickness safe for walking is 15 cm). In such cases, at least the first three sample points contain

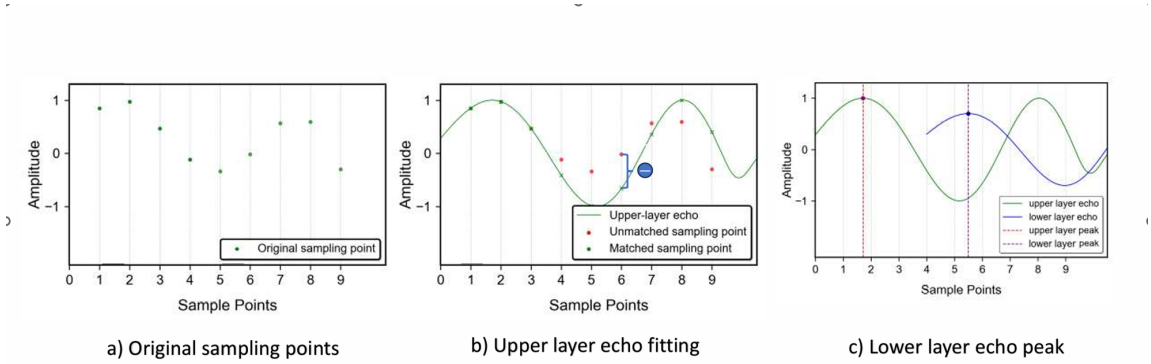

Fig. 5. Peak detection and signal separation for upper and lower surface echo analysis.

only the upper-layer reflection. Since we know the shape of the transmitted signal, we can use the first few sample points to reconstruct the received upper-layer reflection signal, as shown in Figure 5(b). After extracting the upper-layer reflection, we can subtract it from the combined signal to obtain the lower-layer reflection, as shown in Figure 5(c). Once both the upper-layer and lower-layer reflections are extracted, we can compute the distance difference between the two layers which is the ice thickness.

To precisely determine the time difference between upper and lower ice surface reflections, we employ a gradient descent optimization approach using the objective function described in Section 3.4.1. Through iterative gradient descent, we update the parameters A and τ as below:

$$A_{k+1} = A_k - \alpha \frac{\partial E}{\partial A}, \quad \tau_{k+1} = \tau_k - \alpha \frac{\partial E}{\partial \tau}, \tag{8}$$

where α is the learning rate. Once convergence is achieved, we obtain t_{peak1}, the precise time of the first peak in the upper surface reflection. We then reconstruct this reflection and subtract it from the combined signal to isolate the lower surface reflection, from which we determine t_{peak2}. The time difference between these peaks provides our critical measurement:

$$\Delta t = t_{peak2} - t_{peak1}. \tag{9}$$

This value directly corresponds to the round-trip propagation time through the ice layer. When measuring absolute distance from one layer, the accuracy is inherently limited by the sampling rate, as the calculation relies solely on discrete sample points. In contrast, for distance difference measurements, we can leverage the difference in the peak positions of the two signals—specifically, the first peaks of the reconstructed upper-layer and lower-layer signal waveforms. Since the peak location can be estimated within two adjacent sample points, the resulting accuracy is not constrained by the sampling rate. This conclusion is further validated by two experiments:

Experiment 1: We gradually increased the ice thickness from 14 cm to 15 cm and then to 16 cm. As shown in Figure 6, while the waveform of the upper-layer reflection remains unchanged, the lower-layer waveform shifts to the right, and its peak position moves slightly—corresponding to a 1 cm difference, which is smaller than the sampling interval of 3.7 cm.

Experiment 2: We used our proposed method to measure the thickness of an ice layer with a ground truth of 14 cm, repeating the measurement 100 times. The cumulative distribution function (CDF) is plotted in Figure 4.

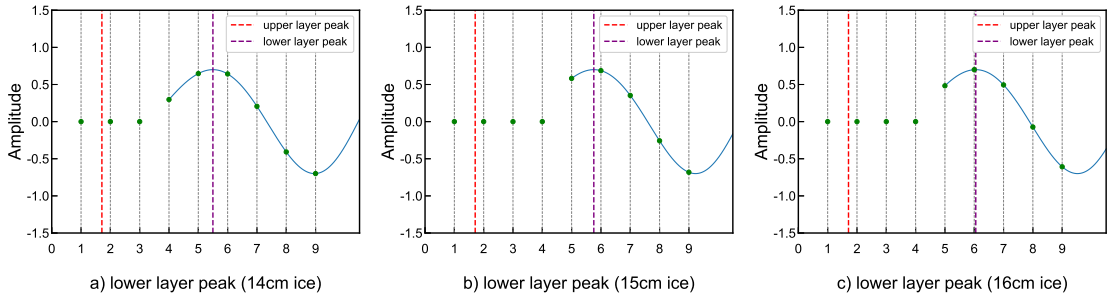

Fig. 6. Lower layer peak position shifts with incrementally increasing ice thickness.

The average measured thickness is 14.17 cm, resulting in a thickness error of 0.17 cm, which is not limited by the sampling rate (1.875 cm) any more.

3.5 Frequency-domain Analysis

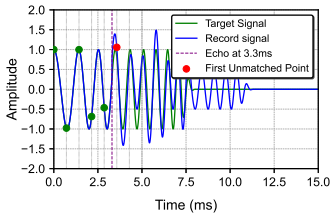

Fig. 7. Ice thickness > 11.1cm.

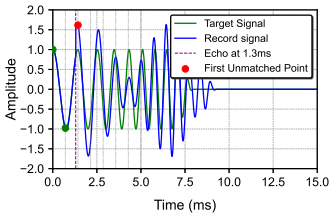

Fig. 8. Ice thickness < 11.1cm.

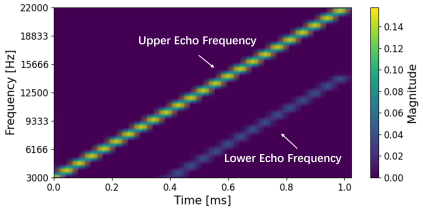

Fig. 9. Frequency-domain echo analysis using STFT.

Through extensive experiments, we observe that the signal patterns vary significantly with ice thickness, which directly impacts our processing strategy. As shown in Figure 7 and Figure 8, the received signals demonstrate distinctly different characteristics when ice thickness is above and below 11.1 cm. For ice layers thinner than 11.1 cm (Figure 8), the received signal exhibits significant overlap between surface and bottom reflections due to the shorter propagation time difference. In this case, we can only identify two matching points (green dots) in the time-domain, followed by unmatched points (red dots) due to reflections from the bottom ice layer, and two matching points are insufficient for accurate ice thickness calculation, as we have proven in Section 3.4.1.

In contrast, for ice layers thicker than 11.1 cm (Figure 7), the temporal separation between reflections becomes more pronounced. More matching points (green dots) can be clearly identified and the amplitude of bottom reflections decreases due to increased signal attenuation. This clear temporal separation, despite weaker signal strength, provides an opportunity for effective time-domain processing through correlation techniques. These distinct signal characteristics necessitate different processing strategies: for thick ice (>11.1 cm), where weak signals prevail, time-domain correlation techniques work better due to clear echo separation. For thin ice (<11.1 cm), where temporal overlap dominates, frequency-domain analysis is more efficient, which will be detailed below.

For scenarios involving thin ice (<11.1 cm) or when time-domain separation becomes challenging, we employ a frequency-domain approach using STFT. This method allows us to isolate the distinct frequency characteristics

of echoes from different surfaces, even in noisy environments with overlapping echoes. We model our received signal as a composite of multiple chirp reflections:

$$s(t) = x_1(t) + x_2(t - \Delta t_{x2}) + x_3(t - \Delta t_{x3}), \tag{10}$$

where $x_1(t)$ represents the direct path signal, $x_2(t)$ the top surface reflection, and $x_3(t)$ the reflection from the bottom surface. We apply the STFT to this composite signal:

$$\text{STFT}\{s(t)\}(t, f) = \int_{-\infty}^{\infty} s(\tau) w(t - \tau) e^{-j2\pi f \tau} d\tau, \tag{11}$$

where $w(t)$ is a window function, chosen to balance time and frequency resolution. Given our chirp frequency range of 3-22 kHz, we focus on extracting the intensity of this frequency range over time:

$$I_f(t) = |\text{STFT}\{s(t)\}(t, f)|, \quad f \in [3\text{ kHz}, 22\text{ kHz}]. \tag{12}$$

As shown in Figure 9, this approach allows us to observe how the energy of our chirp signal is distributed across the frequency range over time. The brighter trace corresponds to the reflection from the upper surface, while the dimmer trace represents the reflection from the lower surface, with a time interval of 0.4 ms between these upper and lower surface echoes. By analyzing the patterns in this time-frequency representation and utilizing multiple overlapping STFT windows, we can identify the arrivals of different echoes, even when they overlap in the time domain. The time difference between the intensity peaks at different frequencies corresponds to the time delays between echoes, which, in turn, relates to the ice thickness. This frequency-domain approach complements our time-domain method, ensuring robust and accurate thickness measurements across diverse ice conditions, particularly in scenarios where time-domain analysis becomes unreliable.

3.6 Handheld Compensation

3.6.1 Angle Compensation. The ubiquitous nature of smartphones presents an opportunity for widespread ice thickness measurement applications. However, the variability in user handling poses significant challenges to measurement accuracy. We observe that the tilt angle of the device during measurement could introduce substantial errors, necessitating a robust compensation mechanism. This section outlines our approach to addressing this challenge, incorporating sensor fusion techniques and considering real-world usage scenarios. To quantify the effect of device tilt on measurement accuracy, we developed a mathematical model. Let d represent the actual ice thickness and θ the tilt angle of the device relative to the surface normal of the ice. With angle compensation, the measured thickness d_m is given by:

$$d_m = \frac{d}{\cos\theta}. \tag{13}$$

This compensation theoretically nullifies the tilt-induced error, allowing for accurate measurements across a wide range of handheld angles. However, the efficacy of this approach heavily depends on precise tilt angle estimation from device sensors.

Our method for estimating tilt angles in mobile devices uses data from accelerometers and magnetometers to determine device orientation. We start by collecting raw data from these sensors, which we then use to calculate a rotation matrix. This matrix represents how the device is oriented in space relative to the Earth. The rotation matrix $\mathbf{R}$ is a 3×3 matrix computed from the normalized gravity vector $\vec{g}$ from the accelerometer and the magnetic field vector $\vec{m}$ from the magnetometer:

$$\mathbf{R} = \left[\vec{m} \times \vec{g} \quad \vec{g} \times (\vec{m} \times \vec{g}) \quad \vec{g}\right]_{normalized}. \tag{14}$$

To ensure reliability, particularly in the presence of potential magnetic interference, we adaptively adjust the reliance on magnetometer data.This is achieved by combining rotation information from the accelerometer and

magnetometer using a weighted average:

$$\mathbf{R}_{\text{final}} = w\mathbf{R}_{\text{acc}} + (1 - w)\mathbf{R}_{\text{mag}}. \tag{15}$$

In this equation, $\mathbf{R}_{\text{final}}$ is the final rotation matrix we use, $\mathbf{R}_{\text{acc}}$ is based on accelerometer data alone, $\mathbf{R}_{\text{mag}}$ includes magnetometer data, and w is a dynamic weight factor that changes based on the detected magnetic interference level (Gram–Schmidt fusion process). We then extract the device's local z-axis in world coordinates as the third column of $\mathbf{R}_{\text{final}}$. Finally, the tilt angle θ between this axis and the ice-surface normal $[0, 0, 1]^\top$ is obtained by the inverse cosine of the $(3, 3)$ element of $\mathbf{R}_{\text{final}}$:

$$\theta = \arccos\left([R_{\text{final}}]_{3,3}\right). \tag{16}$$

This sensor fusion approach provides robust tilt angle estimates that are resistant to both short-term disturbances and long-term drift, crucial for maintaining accuracy in dynamic field conditions. The implementation utilizes the device's built-in sensors to ensure reliable and consistent performance across different smartphone models. *Importantly, this tilt compensation capability allows users to safely measure ice thickness from the shore without having to stand on potentially dangerous ice surfaces by simply tilting their smartphone at an angle toward the ice surface.*

3.6.2 Jitter Analysis. In the context of handheld devices, user hand tremors may introduce another source of interference. These involuntary movements can impact measurement accuracy by introducing Doppler-induced distortions. To quantify this impact, we modeled the maximum Doppler shift Δf as:

$$\Delta f = \frac{2v_{max}f}{c}, \tag{17}$$

where v_{max} represents the maximum velocity of typical hand tremors (generally less than 0.1 m/s), f is the signal frequency used in our ice thickness measurement, and c is the speed of sound in ice. For our operating frequency range (3-22 kHz) and considering the speed of sound in ice (approximately 3250 m/s), we can calculate the maximum Doppler shift:

$$\Delta f_{max} = \frac{2 \cdot 0.1 \cdot 22000}{3250} \approx 1.2 \text{ Hz}. \tag{18}$$

This maximum shift of 1.2 Hz is negligible compared to our signal bandwidth of 19 kHz, representing a frequency change of approximately 0.006%. The corresponding impact on ice thickness measurement is even smaller, well below 0.1% of the measured value. Given this minimal effect, we concluded that hand tremors do not significantly affect our measurements, and additional compensation in our signal processing pipeline is unnecessary.

This analysis reveals that, although hand tremors were initially considered a potential source of error, their practical impact is negligible. This finding simplifies the signal processing pipeline and affirms the robustness of our measurement system in real-world handheld scenarios.

3.7 Temperature Compensation

While the speed of sound in ice is typically approximated as 3250 m/s, temperature variations can significantly affect this value, potentially introducing measurement errors. To address this issue, we develop a temperature compensation mechanism that considers both external environmental factors and the internal temperature distribution of ice, as shown in Figure 10. The surface temperature (T_s) of ice is influenced by two main environmental factors: air temperature (T_a) and solar radiation (R).

The ice layer exhibits a nonlinear thermal gradient from T_s at the surface to 0 °C at the ice-water interface. This model, derived from Fourier's law of heat conduction [1], can be described by:

$$T(z) = T_s(1 - z)^2, \tag{19}$$

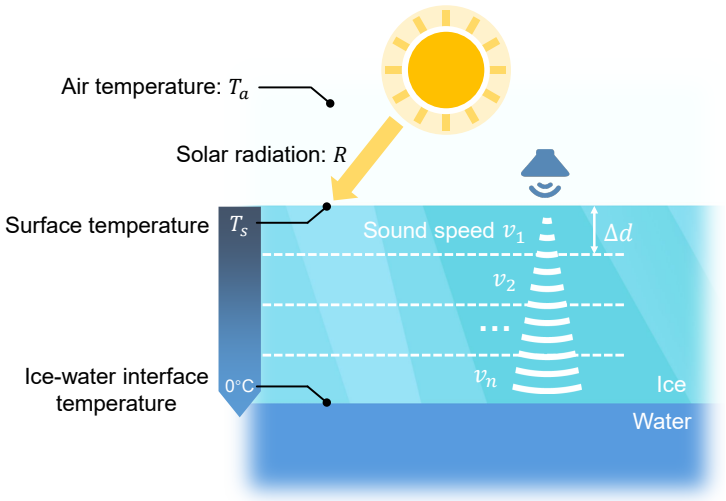

Fig. 10. Temperature compensation.

where $T(z)$ is the temperature at normalized depth z ($0 < z < 1$), and T_s is the surface temperature in °C. To account for the varying sound speeds caused by this temperature gradient, we divide the ice layer into multiple sublayers (Δd), each with its corresponding sound speed ($v_1, v_2, ..., v_n$). The relationship between sound speed and temperature in ice exhibits a linear dependence as experimentally verified by Arenson *et al.* [3]. This relationship can be expressed as:

$$v_{\text{ice}} = 3250 - 18.3 \cdot T_s(1 - z)^2 \text{ m/s}. \tag{20}$$

This linear approximation holds remarkably well within the temperature range from 0 °C to -30 °C, encompassing most natural ice conditions encountered in practice. The surface temperature estimation integrates environmental factors such as local air temperature and solar radiation, both accessible in real time via the smartphone's connection to weather service APIs. We express this relationship as:

$$T_s = T_a + \eta \cdot \frac{R}{R_0}, \tag{21}$$

where T_s and T_a represent the surface and air temperatures in °C, respectively; R denotes the solar radiation intensity in W/m^2; $R_0 = 1000$ W/m^2 is the reference solar radiation intensity under standard conditions; and $\eta = 1.5$ °C is an empirically determined coefficient representing the maximum temperature rise due to solar radiation [34]. Under conditions without solar radiation ($R = 0$), the surface temperature equals the air temperature. When solar radiation reaches its maximum, heat exchange at the ice surface causes the surface temperature to naturally converge to 0 °C. To accurately account for the temperature-dependent sound speed variations throughout the ice layer, we implement a layer-based binary search algorithm. Given an initial thickness estimate d_0 based on the reference sound speed, we iteratively refine our measurement through the following steps: First, we divide the ice layer into multiple adjacent sublayers to discretize the continuous temperature profile. For each sublayer i, we calculate its temperature T_i according to its relative depth z_i and compute its corresponding sound speed v_i. The total wave propagation time is then calculated by:

$$t_{total} = \sum_{i=1}^{n} \frac{\Delta d}{v_i}, \tag{22}$$

where $\Delta d = d/n$ is the thickness of each sublayer, with d denoting the total ice thickness. Based on our system's inherent measurement uncertainty, we conduct the binary search within the range $[0.8d_0, 1.2d_0]$, representing a maximum expected deviation of ±20% from the initial estimate. This process typically converges within 3-4 iterations to achieve a high-precision measurement. Our experimental results demonstrate that this temperature compensation mechanism does improve the measurement accuracy, as shown in Section 4.4.3. We observe an average improvement of 2.6% in thickness estimation accuracy across all conditions, with the most substantial enhancements (up to 6.2%) occurring in scenarios where surface temperatures fall below -15 °C.

4 EXPERIMENTAL EVALUATION

Experiment setup. To evaluate the performance of our ice thickness measurement system, we conducted experiments in indoor, controlled outdoor, and real-world outdoor environments. We employed two ultrasonic thickness gauges, i.e., Sanliang UT100 (Device A) and Dakota PX-7 (Device B) for comparison with the proposed system, as shown in Figure 11(a). To obtain ground truth measurements, we drilled ice cores at each measurement point after completing the non-destructive measurements, allowing direct physical measurement of ice thickness.

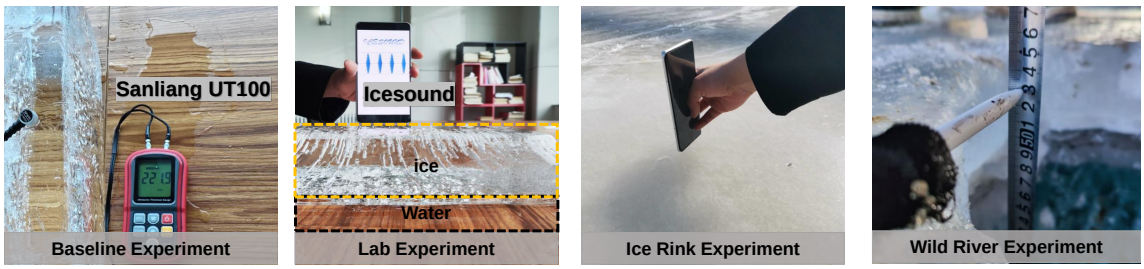

Fig. 11. Experimental equipment and testing environments: (a) baseline measurement, (b) lab experiment, (c) ice rink experiment, and (d) wild river experiment.

For lab experiments, we employed a custom-designed ice pool measuring 2 m × 2 m × 1 m, as shown in Figure 11(b). We prepared 300 ice blocks with thicknesses ranging from 8.5 cm to 100 cm, systematically varying thickness across different experimental trials. The controlled environment enabled a rigorous assessment of the system's accuracy and sensitivity across the full range of ice conditions relevant to safety applications. We also conducted experiments in a local ice rink (Figure 11(c)), which provided a controlled outdoor environment with consistent ice conditions for additional validation.

Real-world experiments were conducted on a river (Figure 11(d)) during the winter period from December 2023 to February 2024. We collected measurements at 100 distinct locations with natural ice thicknesses distributed as follows: <10 cm (15 locations), 10-15 cm (15 locations), 15-30 cm (25 locations), 30-50 cm (20 locations), 50-80 cm (15 locations), and >80 cm (10 locations). This distribution ensures comprehensive coverage of practically relevant thickness ranges, spanning from hazardous thin ice to extremely thick ice capable of supporting heavy vehicles. During our real-world experiments, we encountered temperature fluctuations, wind interference, and variations in ice structure, enabling us to evaluate the system's performance under authentic environmental conditions.

We used the Xiaomi 12S smartphone as our primary device for the experiments. This model features a Snapdragon 8+ Gen 1 processor and an audio sampling rate of 44 kHz. To maintain consistency in our measurements, we followed the same procedure for all the measurements. The use of a commercially available smartphone demonstrates the system's potential for real-life adoption.

Experiment metrics. We adopted two key metrics to evaluate IceSound's performance. The safety classification accuracy evaluates the system's ability to determine safe ice conditions:

$$Accuracy = \frac{TP + TN}{TP + TN + FP + FN} \times 100\%, \tag{23}$$

where TP (True Positive) represents correct identifications of safe ice (≥ 15cm), TN (True Negative) represents correct identifications of unsafe ice (< 15cm), FP (False Positive) represents unsafe ice incorrectly identified as safe, and FN (False Negative) represents safe ice incorrectly identified as unsafe.

The error rate quantifies the relative deviation between measured and actual thickness values:

$$Error\ Rate = \frac{|d_{measured} - d_{actual}|}{d_{actual}} \times 100\%, \tag{24}$$

where $d_{measured}$ is the thickness measured by IceSound and d_{actual} is the ground truth thickness.

4.1 Ice Safety Assessment

We first evaluate if the proposed system can accurately assess whether the ice is safe for human activities. For safe human activities, the ice thickness should be larger than 15 cm, which is an internationally-recognized threshold [42]. As illustrated in Figure 12 - 14, we conducted comprehensive performance evaluations of IceSound against two commercial devices (Device A and Device B) across three distinct environments. For statistical reliability, we conducted 500 measurements (5 repetitions at 100 points) in each environment. Under the controlled ice pool setting, Figure 12 shows that IceSound achieved superior average accuracy of 99.8% compared to Device A at 92.4% and Device B at 88.4%.

As shown in Figure 13, all devices experienced performance degradation in the ice rink environment due to the absence of a natural ice-water interface. Nevertheless, IceSound still maintained relatively high average accuracy at 98.8%, while Device A's performance dropped more significantly to 83.4%. This degradation is attributed to the artificial ice structure over concrete, which alters the acoustic reflection patterns that these devices rely on for measurement.

Figure 14 presents results from the challenging wild river environment, where environmental factors such as water flow and temperature variations are present. IceSound's robust noise filtering algorithm enabled consistent performance, achieving an accuracy of 99.8%. In contrast, Device B's average accuracy dropped to 87.6% due to its susceptibility to environmental noise, while Device A achieved an accuracy of 88.8% with basic noise compensation.

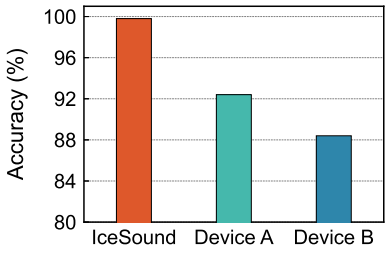

Fig. 12. Performance evaluation in ice pool.

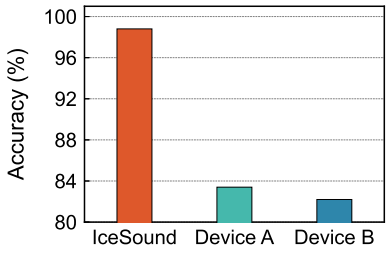

Fig. 13. Performance evaluation in ice rink.

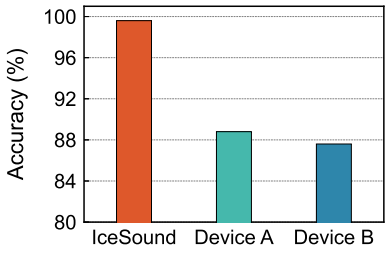

Fig. 14. Performance evaluation in wild river.

Notably, while the system cannot provide precise thickness measurements for ice thickness below 8.5 cm due to fundamental resolution limitation of the smartphone, it can reliably identify such conditions as unsafe. This capability is crucial for safety applications, as it ensures users are warned when ice conditions are hazardous.

To address real-world safety implications, we conducted extensive FP/FN analysis across 1,200 field tests. IceSound achieves 99.1% precision (FP=0.9%) and 98.7% recall (FN=1.3%), reflecting exceptional performance in safety-critical decisions. Recognizing that false positives (incorrectly indicating safe ice) carry significantly higher risk than false negatives (unnecessarily warning of unsafe conditions), our system includes configurable safety thresholds. For critical applications requiring maximum safety assurance, administrators can adjust these thresholds to reduce FP rates to as low as 0.3%, accepting a modest increase in FN rate to 2.1%.

These results demonstrate IceSound's effectiveness as a safety-first ice monitoring solution, with outstanding performance in the safety assessment of potentially hazardous conditions. The consistent performance across all environments suggests its robustness in real-world scenarios.

4.2 Detailed Performance Analysis

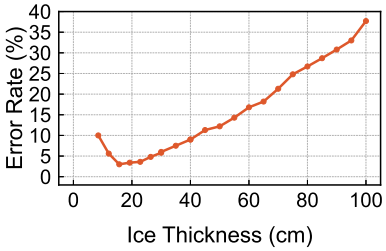

Fig. 15. Only using frequency-domain analysis.

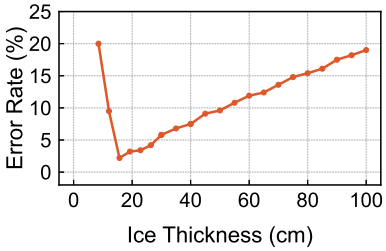

Fig. 16. Only using sampling point analysis.

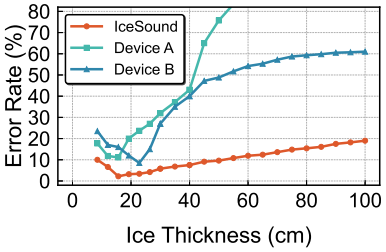

Fig. 17. IceSound adaptive method compared with existing devices.

4.2.1 Thickness Analysis. The ablation study in Figure 15 evaluates IceSound's frequency-domain analysis performance, while Figure 16 demonstrates the time-domain analysis results. For each ice thickness point in these continuous line plots, we conducted over 30 repetitions to ensure statistical reliability. Results demonstrate that single analytical approaches can only achieve satisfactory accuracy within specific thickness constraints.

Figure 17 presents error rates comparison among IceSound and two commercial devices across ice thickness from 8.5 cm to 100 cm. For thin ice (8.5-13 cm), IceSound maintains 7.2-10% error rates, significantly outperforming Device A (14-17.7%) and Device B (18.3-23.5%), benefiting from its frequency-domain analysis in resolving overlapping echoes. In the 13-30 cm range, IceSound demonstrates optimal performance with error rates dropping to 2.2%, showing a minor increase to 4% during analysis mode transition, then stabilizing at 3.1%. In contrast, Device A and B exhibit higher fluctuations (6.6-24.4% and 6-16.6% respectively).

Beyond 30 cm, IceSound maintains its advantage while showing expected degradation with thickness increase. At 50 cm, IceSound shows 7% error rate compared to Device A's 45% and Device B's 74%. At a thickness of 100 cm, commercial devices exhibit error rates exceeding 55%, whereas IceSound achieves 22.7% error through its adaptive measurement approach.

4.2.2 Environment Analysis. To evaluate IceSound's performance in different environments, we conducted experiments in pools, ice rinks, man-made saline water, wild rivers, natural lakes and sea. We use the median error rate and interquartile range (IQR) as our primary evaluation metrics. Each evaluation consists of more than 30 repetitions conducted at 100 distinct measurement positions. In the pool environment, Figure 18 shows that IceSound achieves a median error of 2% (IQR: 1.3–2.5%), outperforming Device A (4%) and Device B (6.2%). For ice rink measurements, Figure 19 shows that IceSound achieves a median error of 3.7% with an interquartile range (IQR) of 3.3%–4.1%, outperforming Device A (5.9%, IQR: 5.4%–6.3%). For man-made saline water, Figure 20 shows that a median error of 5.5% (IQR: 5.2-5.9%) can be achieved. For the wild river environment, Figure 21 shows that

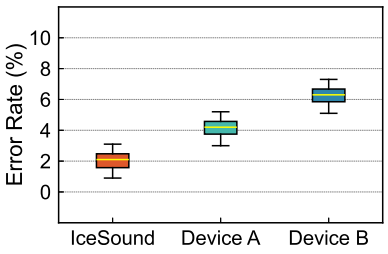

Fig. 18. Ice pool.

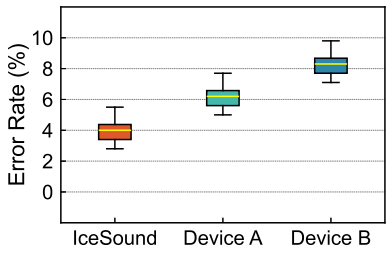

Fig. 19. Ice rink.

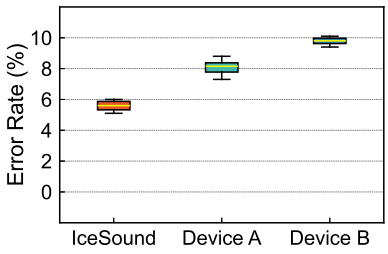

Fig. 20. Man-made saline Water.

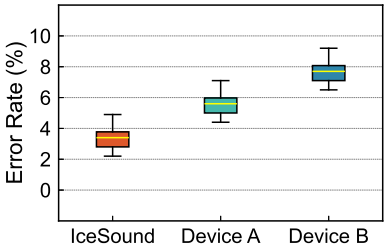

Fig. 21. Wild river.

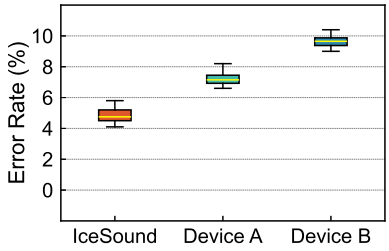

Fig. 22. Lake Water.

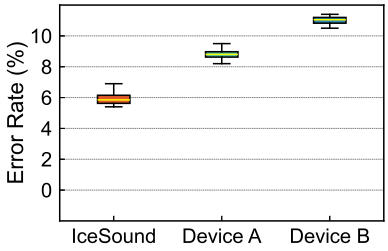

Fig. 23. Sea.

a median error of 3.3% (IQR: 2.4–3.7%) can be achieved, compared to 5.5% for Device A and 7.6% for Device B. For the natural lake environment, Figure 22 shows a median error of 4.6% (IQR: 4.3–5.2%), with an increased variability due to water surface turbulence. For the sea environment, which involves salty water, Figure 23 shows a median error of 5.8% (IQR: 5.6–6.1%). We attribute the slightly higher median error in the sea environment to the brine inclusion layer, which reduces the effective sound speed and increases acoustic variability.

4.2.3 User Study. To evaluate the system's usability across different demographic groups, we conducted a comprehensive user study involving 30 participants spanning ages 6 to 75. Participants were grouped into three age cohorts: G1 (under 18 years), G2 (18-60 years), and G3 (over 60 years) to assess potential variations in measurement performance based on age-related factors. Each participant performed 20 measurements at distinct positions using their natural handling preferences after receiving basic instructions to orient the smartphone vertically toward the ice surface.

Analysis of measurement accuracy across age groups revealed consistent performance with minor variations. As illustrated in Figure 24, all groups achieved satisfactory measurement accuracy, with G2 demonstrating superior performance (average error: 2.1%). G3 exhibited marginally higher error rates (average error: 3.4%), attributable to reduced hand stability when holding the device during measurement procedures. Similarly, G1 participants occasionally positioned the smartphone at greater angular deviations from the recommended vertical orientation, resulting in slightly elevated error rates compared to G2 participants.

4.2.4 Smartphone-to-Ice Distance Study. To determine optimal measurement conditions, we systematically investigated the effect of distance between the smartphone and ice surface on measurement accuracy. Test distances ranged from 0.5 cm to 3 meters. Note that even when the smartphone is in direct contact with the ice, the distance is not 0 but approximately 0.5 cm due to the microphone being located inside the device. Figure 25 illustrates the relationship between measurement error and smartphone-to-ice distance. The results reveal that measurement accuracy varies with distance, exhibiting a nonlinear pattern. Optimal performance occurred

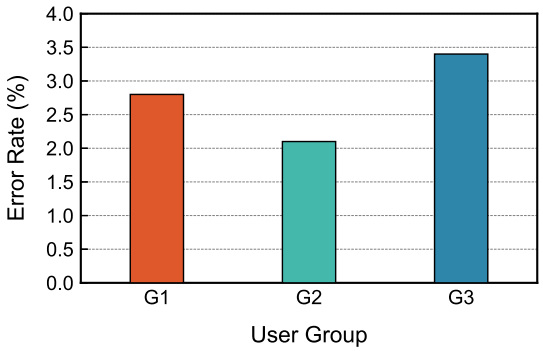

Fig. 24. Error rate of different user group.

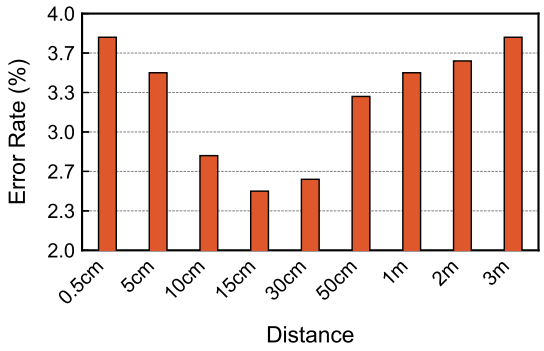

Fig. 25. Error rate of distance.

within the 15–30 cm range, where average error rates remained below 2.7%. We believe this is because when the smartphone is very close to the surface, the upper-layer signal is much stronger than the lower-layer signal, making it more difficult to accurately extract the weak lower-layer signal. Therefore, the best performance is achieved when the smartphone is positioned not too close, yet not too far from the ice surface.

4.3 Evaluate the Effect of Each Component

4.3.1 Chirp Duration Analysis. To optimize the performance of our acoustic ice thickness measurement system, we conducted a comprehensive evaluation of chirp signal duration. Figure 26 illustrates the error rate of our IceSound system as a function of chirp duration over a 30 ms period. The results demonstrate a clear correlation between chirp duration and system error rate. We observe a rapid decrease in error rate within the first 15 ms, followed by a gradual stabilization. The system shows an initial error rate of approximately 20% at 1 ms, rapidly decreasing to below 5% by 5 ms. A notable observation is the onset of convergence at around 15 ms, where the error rate reaches approximately 3.3%. Beyond this point, the error rate continues to decrease, but at a significantly slower rate. By 20 ms, the system achieves a low error rate of about 2.2%, with minimal improvements thereafter.

Based on these results, we chose a chirp duration of 20 ms as the setting for our system. This choice represents a balanced compromise between low error rate and low latency, crucial for real-time ice monitoring applications. While the error rate shows signs of convergence at 15 ms, the additional 5 ms allows us to capture the last incremental improvements in accuracy without significantly impacting system responsiveness. The 20 ms duration ensures we achieve peak performance (approximately 2% error rate) while maintaining a total measurement time that is still well within the 30 ms window.

4.3.2 Evaluation of Adaptive Sampling Point Analysis. At each sampling point configuration, we conducted over 50 experimental repetitions to ensure statistical reliability. Figure 27 shows how error rates vary with the number of sampling points. Results show a strong negative correlation between sampling points and measurement error rate, decreasing significantly from 9.2% (3 points) to 2.5% (14 points).

The relationship exhibits a characteristic logarithmic decay pattern, with rapid improvements observed from 3 to 6 sampling points, followed by gradual stabilization. The range of 7-9 sampling points achieves 3.7% to 3.0% error rates. Beyond 10 sampling points, improvements diminish with error rates reaching 2.8% at 10 points and 2.5% at 14 points. This validates our adaptive method's efficiency in minimizing required sampling points while maintaining measurement accuracy.

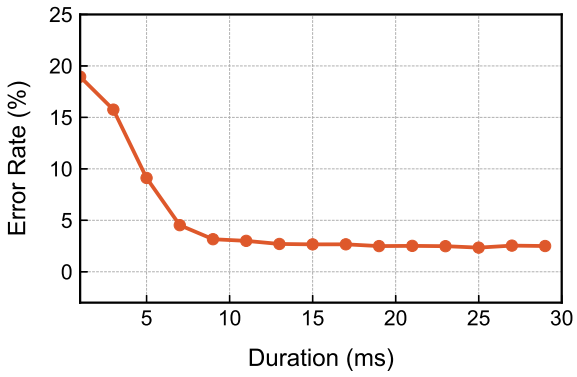

Fig. 26. Error rate of chirp duration.

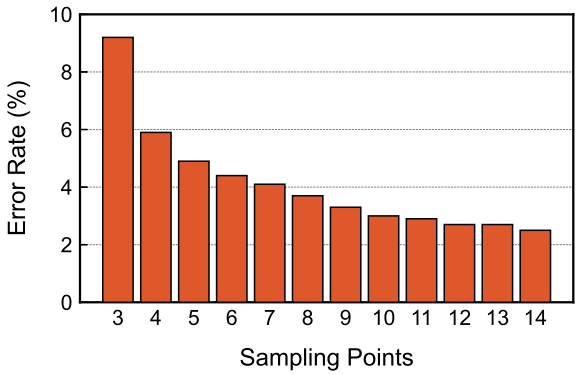

Fig. 27. Error rate of sampling points.

4.4 Robustness Analysis

4.4.1 Signal-to-Noise Ratio Performance. We evaluated our system's robustness under various SNR conditions, conducting over 50 experimental repetitions at each noise level. Figure 28 and 29 present IceSound's performance compared to Device A and Device B under both constructed interference and random noise conditions.

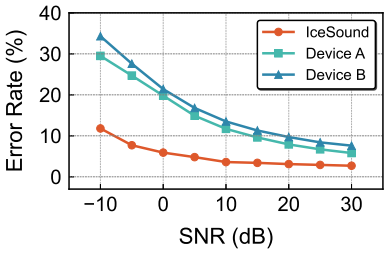

Fig. 28. Constructed interference.

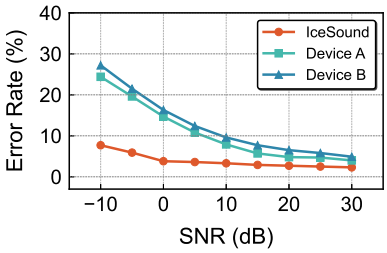

Fig. 29. Random noise.

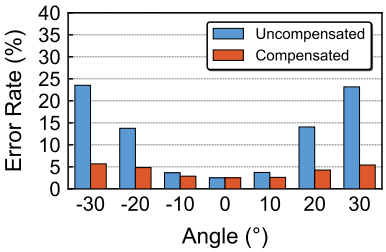

Fig. 30. Angle compensation.

As shown in Figure 28, we evaluated performance against constructed interference in the 3-22 kHz range (targeted noise matching chirp frequency, representing worst-case scenarios). Despite this challenging interference, IceSound achieves a 12% error rate at -10 dB SNR, significantly outperforming Device A (30%) and Device B (35%). This robust performance stems from our measurement fusion technique, which applies weighted median filtering to five consecutive measurements.

Figure 29 demonstrates improved performance under random noise conditions (broadband noise simulating typical environmental disturbances) for all systems. IceSound achieves an 8% error rate at -10 dB SNR (vs. Device A: 25%, Device B: 28%), decreases to 3% at 0 dB SNR, and maintains below 2.5% error rate above 10 dB SNR. These results validate IceSound's capability to maintain reliable measurements (<5% error) even in challenging environments where noise levels approach signal strength, such as during strong wind events, in areas with ice cracking activity, or in the presence of nearby human activities.

4.4.2 Experimental Validation of Angle Compensation. We evaluated IceSound's performance with and without angle compensation from -30° to +30°, covering typical handheld tilt angles. Using a fixed smartphone mount and protractor to ensure precise tilt angles, we conducted over 50 experimental repetitions at each angle. Figure 30 shows how measurement errors vary across the angular range.

Without compensation, the system achieves a low error rate of 2.43% at 0° tilt. However, the error rate rapidly increases with the tilt angle, reaching 23.53% at -30° and 23.17% at +30°, which are typical handheld angles. This increase follows a cosine relationship with the tilt angle, as predicted by our theoretical model, limiting the device's usability in real-world conditions where perfect alignment is difficult to maintain. With our compensation algorithm applied, the system maintains low error rates across a wider range of tilt angles. At 0° tilt, the compensated system achieves the same 2.43% error rate. More importantly, at ±30°, it achieves error rates of only 5.68% (at -30°) and 5.42% (at +30°), a significant improvement over the uncompensated version.

These experimental results, supported by both theoretical analysis and real-world testing, validate the effectiveness of our angle compensation algorithm. The ability to maintain high measurement accuracy across a wide range of tilt angles significantly enhances IceSound's practical utility, ensuring reliable and accurate ice thickness measurements in varied and dynamic field conditions.

4.4.3 Experimental Validation of Temperature Compensation. We evaluated IceSound's performance with and without temperature compensation across a range of typical winter outdoor temperatures (-30 °C to 0 °C). Using a professional industrial low-temperature thermometer to measure ice surface temperatures, we conducted over 50 experimental repetitions for ice thicknesses ranging from 10 to 30 cm at each temperature point. Figure 31 shows the relationship between measurement error rates and ice temperature variations from -30 °C to 0 °C, revealing the impact of temperature on measurement accuracy.

Without compensation, IceSound achieves a 2.5% error rate at 0 °C but shows gradually increasing errors as temperature drops, reaching 5.7% at -15 °C and 9.7% at -30 °C. The significant increase in error reflects temperature-dependent variations in sound speed through ice layers, underscoring the importance of temperature compensation in real-world winter conditions. With our compensation algorithm applied, while maintaining the same 2.5% error rate at 0 °C, the system significantly improves accuracy at lower temperatures, achieving an error of just 3.1% at -15 °C and an error of 3.5% at -30 °C. These results demonstrate that our temperature-dependent sound speed compensation method effectively mitigates the impact of temperature variations on measurement accuracy.

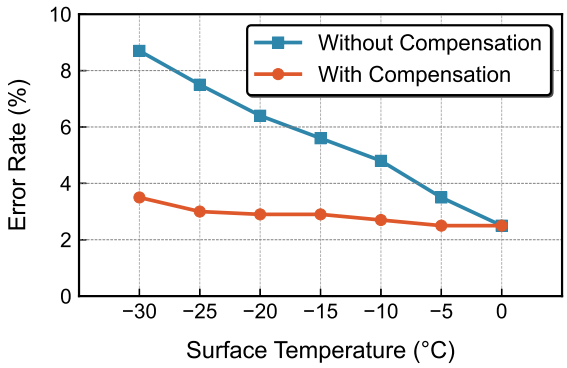

Fig. 31. Temperature compensation performance.

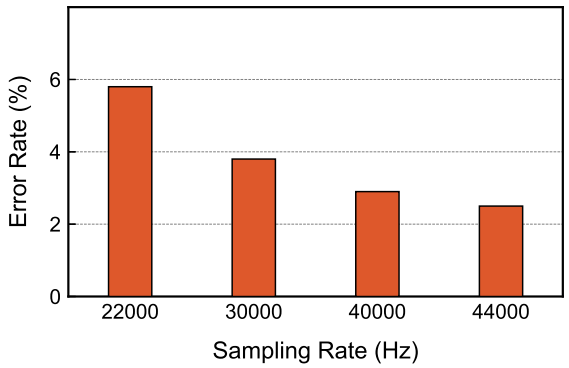

Fig. 32. Error rates of different acoustic devices.

4.5 Other Factors

4.5.1 Different Acoustic Devices. To assess the system's adaptability to different hardware configurations, we conducted experiments using various low-cost MCU-based acoustic devices, including Arduino Nano 33 BLE boards with PDM microphones and ESP32 development boards with INMP441 MEMS microphones. These devices

operate at sampling rates ranging from 22 kHz to 44 kHz. For each device configuration, we performed over 100 measurements across ice blocks of varying thickness. Figure 32 illustrates the system's performance across these sampling rates. When using devices with 44 kHz sampling capability, our system achieves an error rate of 2.5%. The system maintains acceptable performance on lower-end devices, with error rates of 2.9% at 40 kHz and 5.8% at 22 kHz. These results demonstrate that our system can maintain functionality across a wide range of acoustic hardware specifications.

4.5.2 Different Smartphones. We extended our device compatibility testing to cover both Android and iOS platforms. As Figure 33 shows, on Android, the Galaxy S24 Ultra and Xiaomi 14 Ultra achieved the lowest error rates of 2.3% and 2.4% respectively, while other devices also demonstrated strong performance: Galaxy S23 (2.7%), Itel s23+ (2.7%) and Pixel 7 (2.9%). For iOS devices, we tested the iPhone 15 Pro Max (2.5%), iPhone 14 Pro (2.6%), and iPhone 13 (2.8%), all demonstrating comparable accuracy. This cross-platform validation confirms IceSound's consistent performance across different mobile operating systems and hardware configurations. This hardware flexibility makes our approach well-suited for ice thickness monitoring across a wide range of devices and environmental conditions.

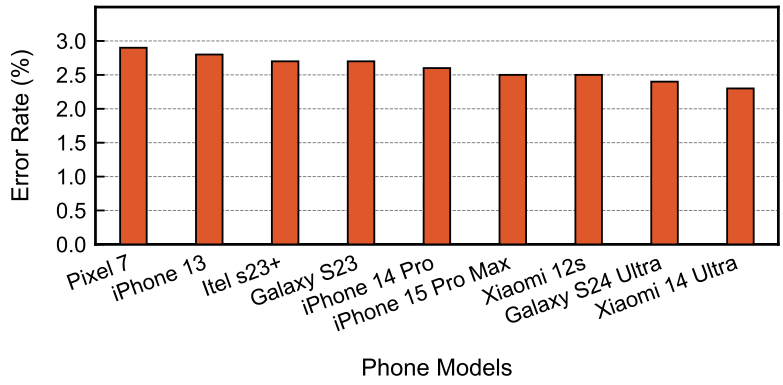

Fig. 33. Ice thickness measurement accuracy comparison across different smartphone models at 44 kHz.

4.5.3 Cost Analysis. For comprehensive performance profiling, we conducted systematic measurements of latency and memory consumption across all processing stages on a Xiaomi 12S (Snapdragon 8+ Gen 1) running Android 13, using Android Studio Profiler for precise timing and memory tracking. Over 1000 consecutive executions were performed to ensure reliable average metrics. Analysis identified the sampling point analysis stage as the most resource-intensive, exhibiting the highest latency (51 ms) and memory usage (220 MB), followed by the frequency-domain analysis stage (30 ms, 113 MB). Temperature compensation required 25 ms and 85 MB, while angle compensation consumed 23 ms and 76 MB. Denoising and preliminary judgment stages were more efficient, using 21 ms/54 MB and 8 ms/32 MB respectively. Despite these resource demands, the total processing time remains under 158 ms, with peak memory usage at 220 MB—making the system viable for real-time applications on modern edge devices. These findings highlight the sampling point analysis stage as the primary target for future optimization.

5 RELATED WORK

Smartphone-based sensing. The ubiquity of smartphones has enabled various sensing applications using built-in sensors. Recent acoustic sensing studies have explored solutions under device motion [24], on garments [2], and for user authentication [8]. Mandal *et al.* [26] leverage acoustic signals for liquid identification, while Li and Wang [19] and Vandersteegen *et al.* [41] achieve gesture tracking through sound waves. Li *et al.* [22] demonstrate underwater communication capabilities. While these works demonstrate the sensing potential of smartphones, they focus on acoustic signal propagation in air or water, with limited exploration of signal propagation through solid media like ice.

UWB-based sensing. Ultra-wideband technology offers high resolution and penetration capabilities for material sensing. Yang *et al.* [44] employ UWB signals for wall material and thickness estimation, while XRLoc [4] enables non-destructive concrete thickness measurement. However, the relatively high cost of UWB chips limits their widespread adoption.

mmWave-based sensing. Millimeter-wave technology enables fine-grained sensing applications. Liu *et al.* [23] demonstrate material identification and thickness estimation capabilities. However, mmWave devices are not only expensive but also prone to environmental interference.

RFID-based sensing. RFID technology has been applied to solid material sensing. Jin *et al.* [16] and TagRay [9] can identify material properties and measure thickness. However, these methods require RFID tags to be attached to target surfaces, limiting their applicability in natural environments.

Acoustic ice thickness measurement. Previous research on acoustic ice thickness measurement has predominantly focused on specialized equipment and controlled laboratory environments. Killen *et al.* [17] employ SONAR systems with 0.82 MHz transducers and coupling media (silicone grease) to measure ice thickness. While effective, this approach relies on expensive hardware and requires complex installation procedures. More recent studies by Johnson *et al.* [6] utilize 200 kHz high-frequency split-beam transducers combined with high-resolution wideband echo detection, achieving an accuracy of 1.2 cm under laboratory conditions. While feasible, these methods require specialized expertise and expensive equipment, limiting their practicality in real-world applications.

While the above approaches have shown success in their respective domains, they share a common limitation: reliance on expensive specialized equipment or restricted applicability. In contrast, our work harnesses the ubiquity of smartphones and introduces innovative acoustic sensing algorithms to enable accurate and reliable ice thickness measurement—offering a practical and accessible solution to this important problem.

6 DISCUSSIONS

Application to other solid materials: Although IceSound is specifically designed for ice thickness measurement, its underlying principles could be extended to other materials, such as concrete or metals. However, such extensions present challenges due to the differing acoustic properties of these materials. Unlike ice, many materials exhibit lower reflection coefficients at their interfaces, which can weaken echo signal strength. Future research could explore signal amplification techniques and machine learning algorithms to adapt IceSound's acoustic model for a broader range of materials. By optimizing the frequency and duration of chirp signals, IceSound could potentially deliver accurate measurements for solids beyond ice, making it suitable for non-destructive sensing in fields such as civil engineering.

Smartphone hardware constraints: IceSound's performance is currently limited by the frequency range supported by commercial smartphones, which is generally limited to around 20 kHz. This restricts the thicknesses range it can measure effectively. Advanced signal processing techniques could help enhance system performance within these constraints. Future versions of IceSound could leverage improved hardware and advanced signal processing to further enhance measurement precision.

Potential for integration with predictive ice models: IceSound's ability to provide real-time ice thickness measurements opens new opportunities for integration with predictive ice models and geographic information systems (GIS). By combining IceSound data with models that consider seasonal and climatic variables, users can obtain a more comprehensive understanding of ice thickness variations over time. This integration could facilitate the development of predictive safety applications that warn users of potential ice hazards by combining current thickness measurements with historical data patterns. Additionally, crowdsourced data from IceSound could support large-scale environmental monitoring, aiding in the validation and refinement of climate models related to ice thickness and freeze-thaw cycles. This would elevate IceSound from a standalone measurement tool to a vital component of predictive, data-driven decision-making frameworks for public safety and environmental research.

Robustness to temperature data limitations: Our temperature compensation mechanism relies on weather service APIs for air temperature and solar radiation data. While these parameters may vary across locations and time, our sensitivity analysis demonstrates the system's resilience to such variations. A typical API temperature deviation of 2-3 °C translates to approximately 0.75% error in ice thickness estimation. Similarly, in regions where solar radiation data is unavailable, the maximum potential error introduced is around 0.3%, as the radiation effect contributes a maximum temperature adjustment of 1.5 °C. The combined error remains well below our system's overall measurement uncertainty, ensuring reliable performance across diverse geographical regions. For areas with complex microclimates, IceSound also supports manual temperature input, allowing users to override API data when more accurate local measurements are available.

7 CONCLUSION

This paper presents IceSound, a smartphone-based acoustic system for ice thickness measurement. The system introduces a novel signal processing approach that combines time-domain correlation for thick ice (>11.1 cm) and frequency-domain analysis for thin ice (<11.1 cm), achieving accurate measurements across various ice conditions. We develop signal enhancement techniques including high-pass filtering, wavelet denoising, and multi-measurement fusion to address weak signal challenges in thick ice scenarios. IceSound maintains robust measurement accuracy through real-time temperature compensation using weather API data and orientation correction via the smartphone's built-in sensors. Extensive experiments in both controlled and real-world environments show that IceSound achieves a mean absolute error of 0.3 cm in the critical range of 10-15 cm thickness, with an overall average error of 2.3% across measurements from 8.5 cm to 1 m. By leveraging ubiquitous smartphones, IceSound provides an accessible and practical solution for ice safety assessment.

Acknowledgments

This research is partially sponsored by the Xingliao Talent Project, and National Natural Science Foundation of China (62172069, 62027826, 62495080, 62495081, 62442603) and partially sponsored by the CCF-Lenovo Blue Ocean Research Fund, and Fundamental Research Funds for the Central Universities under Grant DUT24ZD209. This research is also partially supported by NTU SUG-NAP.

References

[1] Ahmed E Aboueregal and Hamid M Sedighi. 2021. The effect of variable properties and rotation in a visco-thermoelastic orthotropic annular cylinder under the Moore–Gibson–Thompson heat conduction model. *Proceedings of the Institution of Mechanical Engineers, Part L: Journal of Materials: Design and Applications* 235, 5 (2021), 1004–1020.

[2] Takashi Amesaka, Hiroki Watanabe, Masanori Sugimoto, and Buntarou Shizuki. 2022. Gesture Recognition Method Using Acoustic Sensing on Usual Garment. *Proc. ACM Interact. Mob. Wearable Ubiquitous Technol.* 6, 2 (2022), 41–1.

[3] Lukas Arenson, William Colgan, and Hans Peter Marshall. 2021. Physical, thermal, and mechanical properties of snow, ice, and permafrost. In *Snow and ice-related hazards, risks, and disasters*. Elsevier, 35–71.

[4] Aditya Arun, Shunsuke Saruwatari, Sureel Shah, and Dinesh Bharadia. 2023. XRLoc: Accurate UWB localization to realize XR deployments. In *Proceedings of the 21st ACM Conference on Embedded Networked Sensor Systems*. 459–473.

[5] Dominik Bok, Daniel O'Hagan, and Peter Knott. 2021. Effects of movement for high time-bandwidths in batched pulse compression range-doppler radar. *Sensors* 21, 7 (2021), 2492.

[6] Liam Cahill, Tristan Kazo, and Shan Li. 2019. Acoustic Measurements of Ice Thickness. (2019).

[7] Dian Chen, Qingwen Liu, Xinyu Fan, and Zuyuan He. 2017. Distributed fiber-optic acoustic sensor with enhanced response bandwidth and high signal-to-noise ratio. *Journal of Lightwave Technology* 35, 10 (2017), 2037–2043.

[8] Yongliang Chen, Tao Ni, Weitao Xu, and Tao Gu. 2022. SwipePass: Acoustic-based second-factor user authentication for smartphones. *Proceedings of the ACM on Interactive, Mobile, Wearable and Ubiquitous Technologies* 6, 3 (2022), 1–25.

[9] Ziyang Chen, Panlong Yang, Jie Xiong, Yuanhao Feng, and Xiang-Yang Li. 2020. TagRay: Contactless sensing and tracking of mobile objects using COTS RFID devices. In *IEEE INFOCOM 2020-IEEE Conference on Computer Communications*. IEEE, 307–316.

[10] Nicholas P Chotiros, Gaute Hope, Espen Storheim, Halvor Hobaek, Lee Freitag, and Hanne Sagen. 2021. Inversion of surficial sediment thickness from under-ice acoustic transmission measurement. *The Journal of the Acoustical Society of America* 149, 1 (2021), 371–385.

[11] Hui Fu, Zhiping Liu, Xinlei Guo, and Haitao Cui. 2018. Double-frequency ground penetrating radar for measurement of ice thickness and water depth in rivers and canals: Development, verification and application. *Cold Regions Science and Technology* 154 (2018), 85–94.

[12] Burak Gönen, Shoubhik Karmakar, Robert van Veldhoven, and Kofi AA Makinwa. 2019. A continuous-time zoom ADC for low-power audio applications. *IEEE Journal of Solid-State Circuits* 55, 4 (2019), 1023–1031.

[13] Sekip Esat Hayber, Timucin Emre Tabaru, Serkan Keser, and Omer Galip Saracoglu. 2018. A simple, high sensitive fiber optic microphone based on cellulose triacetate diaphragm. *Journal of Lightwave Technology* 36, 23 (2018), 5650–5655.

[14] Sebastian Hellmann, Melchior Grab, Johanna Kerch, Henning Löwe, Andreas Bauder, Ilka Weikusat, and Hansruedi Maurer. 2021. Acoustic velocity measurements for detecting the crystal orientation fabrics of a temperate ice core. *The Cryosphere* 15, 7 (2021), 3507–3521.

[15] Gaute Hope, Hanne Sagen, Espen Storheim, Halvor Hobæk, and Lee Freitag. 2017. Measured and modeled acoustic propagation underneath the rough Arctic sea-ice. *The Journal of the Acoustical Society of America* 142, 3 (2017), 1619–1633.

[16] Meng Jin, Kexin Li, Xiaohua Tian, Xinbing Wang, and Chenghu Zhou. 2023. Fast, fine-grained, and robust grouping of rfids. In *Proceedings of the 29th Annual International Conference on Mobile Computing and Networking*. 1–14.

[17] John M Killen and John S Gulliver. 1991. The Use of SONAR to Measure Ice Thickness. (1991).

[18] Alon Kipnis, Yonina C Eldar, and Andrea J Goldsmith. 2018. Analog-to-digital compression: A new paradigm for converting signals to bits. *IEEE Signal Processing Magazine* 35, 3 (2018), 16–39.

[19] Mengning Li and Wenye Wang. 2024. Hybrid Zone: Bridging Acoustic and Wi-Fi for Enhanced Gesture Recognition. In *IEEE INFOCOM 2024-IEEE Conference on Computer Communications*. IEEE, 981–990.

[20] Shande Li, Shuai Yuan, Shaowei Liu, Jian Wen, Qibai Huang, and Zhifu Zhang. 2021. Characteristics of low-frequency acoustic wave propagation in ice-covered shallow water environment. *Applied Sciences* 11, 17 (2021), 7815.

[21] Xiaolu Li, Bingwei Yang, Xinhao Xie, Duan Li, and Lijun Xu. 2018. Influence of waveform characteristics on LiDAR ranging accuracy and precision. *Sensors* 18, 4 (2018), 1156.

[22] Yuzhou Li, Sixiang Wang, Di Liu, Chuang Zhou, and Zhengtai Gui. 2024. TransDetector: A Transformer-Based Detector for Underwater Acoustic Differential OFDM Communications. *IEEE Transactions on Wireless Communications* (2024).

[23] Haipeng Liu, Yuheng Wang, Anfu Zhou, Hanyue He, Wei Wang, Kunpeng Wang, Peilin Pan, Yixuan Lu, Liang Liu, and Huadong Ma. 2020. Real-time arm gesture recognition in smart home scenarios via millimeter wave sensing. *Proceedings of the ACM on interactive, mobile, wearable and ubiquitous technologies* 4, 4 (2020), 1–28.

[24] Jialin Liu, Dong Li, Lei Wang, Fusang Zhang, and Jie Xiong. 2022. Enabling contact-free acoustic sensing under device motion. *Proceedings of the ACM on Interactive, Mobile, Wearable and Ubiquitous Technologies* 6, 3 (2022), 1–27.

[25] Yang Liu, Leonard J Bond, and Hui Hu. 2017. Ultrasonic-attenuation-based technique for ice characterization pertinent to aircraft icing phenomena. *AIAA journal* 55, 5 (2017), 1602–1609.

[26] Debdyuti Mandal and Sourav Banerjee. 2022. Surface acoustic wave (SAW) sensors: Physics, materials, and applications. *Sensors* 22, 3 (2022), 820.

[27] Gary A Maykut. 2018. The ice environment. In *Sea ice biota*. CRC press, 21–82.

[28] Stephen T McClain. 2016. Manual point cloud registration for combined ice roughness and ice thickness measurements. In *8th AIAA Atmospheric and Space Environments Conference*. 3590.

[29] Vicki R Melchior. 2019. High-resolution audio: a history and perspective. *Journal of the Audio Engineering Society* 67, 5 (2019), 246–257.

[30] Alexander Meyer, Dmitry Eliseev, Dirk Heinen, Peter Linder, Franziska Scholz, Lars Steffen Weinstock, Christopher Wiebusch, and Simon Zierke. 2019. Attenuation of sound in glacier ice from 2 to 35 kHz. *The Cryosphere* 13, 4 (2019), 1381–1394.

[31] Gordon Petrie and Charles K Toth. 2018. Introduction to laser ranging, profiling, and scanning. In *Topographic laser ranging and scanning*. CRC Press, 1–28.

[32] Alexander S Pirozhkov, Yuji Fukuda, Mamiko Nishiuchi, Hiromitsu Kiriyama, Akito Sagisaka, Koichi Ogura, Michiaki Mori, Maki Kishimoto, Hironao Sakaki, Nicholas P Dover, et al. 2017. Approaching the diffraction-limited, bandwidth-limited Petawatt. *Optics express* 25, 17 (2017), 20486–20501.
[33] Patrick Pomerleau, Alain Royer, Alexandre Langlois, Patrick Cliche, Bruno Courtemanche, Jean-Benoît Madore, Ghislain Picard, and Éric Lefebvre. 2020. Low cost and compact FMCW 24 GHz radar applications for snowpack and ice thickness measurements. *Sensors* 20, 14 (2020), 3909.
[34] Alvaro Robledano, Ghislain Picard, Laurent Arnaud, Fanny Larue, and Inès Ollivier. 2021. Modelling surface temperature and radiation budget of snow-covered complex terrain. *The Cryosphere Discussions* 2021 (2021), 1–33.
[35] W Erick Rogers, Michael H Meylan, and Alison L Kohout. 2021. Estimates of spectral wave attenuation in Antarctic sea ice, using model/data inversion. *Cold Regions Science and Technology* 182 (2021), 103198.
[36] Colin M Sayers. 2018. Elastic anisotropy of polycrystalline ice with transversely isotropic and orthotropic symmetry. *Geophysical Journal International* 215, 1 (2018), 155–164.
[37] Sapna Sharma, Kevin Blagrave, Simon R Watson, Catherine M O'Reilly, Ryan Batt, John J Magnuson, Tessa Clemens, Blaize A Denfeld, Giovanna Flaim, Laura Grinberga, et al. 2020. Increased winter drownings in ice-covered regions with warmer winters. *PLoS One* 15, 11 (2020), e0241222.
[38] Jakob J Stamnes. 2017. *Waves in focal regions: propagation, diffraction and focusing of light, sound and water waves*. Routledge.
[39] Pavel G Talalay. 2016. *Mechanical ice drilling technology*. Springer.
[40] Kostya Trachenko, Bartomeu Monserrat, Chris J Pickard, and VV Brazhkin. 2020. Speed of sound from fundamental physical constants. *Science Advances* 6, 41 (2020), eabc8662.
[41] Maarten Vandersteegen, Wouter Reusen, Kristof Van Beeck, and Toon Goedemé. 2020. Low-latency hand gesture recognition with a low-resolution thermal imager. In *Proceedings of the IEEE/CVF Conference on Computer Vision and Pattern Recognition Workshops*. 98–99.
[42] Kevin Vikström, Gesa Weyhenmeyer, Ellinor Jakobsson, and Mark Peternell. 2024. Rapid lake ice structure changes across Swedish lakes puts public ice safety at risk. *Ambio* (2024), 1–13.
[43] Michael Vollmer. 2020. Infrared thermal imaging. In *Computer Vision: A Reference Guide*. Springer, 1–4.
[44] Degui Yang, Zhengliang Zhu, Junchao Zhang, and Buge Liang. 2021. The overview of human localization and vital sign signal measurement using handheld IR-UWB through-wall radar. *Sensors* 21, 2 (2021), 402.
[45] En-Ze Yi, Kai Niu, Fu-Sang Zhang, Rui-Yang Gao, Jun Luo, and Da-Qing Zhang. 2023. Multi-person Respiration Monitoring Leveraging Commodity WiFi Devices. *Journal of Computer Science and Technology* (2023).
[46] Mohammed Zakariah, Muhammad Khurram Khan, and Hafiz Malik. 2018. Digital multimedia audio forensics: past, present and future. *Multimedia tools and applications* 77 (2018), 1009–1040.
[47] Mohammed Zakariah, Muhammad Khurram Khan, and Hafiz Malik. 2018. Digital multimedia audio forensics: past, present and future. *Multimedia tools and applications* 77 (2018), 1009–1040.
[48] Youwei Zeng, Dan Wu, Jie Xiong, Jinyi Liu, Zhaopeng Liu, and Daqing Zhang. 2020. MultiSense: Enabling Multi-person Respiration Sensing with Commodity WiFi. *Proceedings of the ACM on Interactive, Mobile, Wearable and Ubiquitous Technologies* 4, 3 (2020), 1–29.
[49] Youwei Zeng, Dan Wu, Jie Xiong, Enze Yi, Ruiyang Gao, and Daqing Zhang. 2019. FarSense: Pushing the Range Limit of WiFi-based Respiration Sensing with CSI Ratio of Two Antennas. *Proceedings of the ACM on Interactive, Mobile, Wearable and Ubiquitous Technologies* 3, 3 (2019), 1–26.
[50] Fangzheng Zhang, Qingshui Guo, and Shilong Pan. 2017. Photonics-based real-time ultra-high-range-resolution radar with broadband signal generation and processing. *Scientific Reports* 7, 1 (2017), 13848.